Supplementary Material for "Direct laser writing for cardiac tissue engineering: a microfluidic heart on a chip with integrated transducers"

R. K. Jayne,[1,2] M. Ç. Karakan,[1,2] Kehan Zhang,[3,4] Christos Michas,[3,2] N. Pierce,[2] D. J. Bishop,[1,5,6,7,8] C. S. Chen,[3,4] K. L. Ekinci,[1,2,*] and A. E. White[1,5,6,8,†]

[1]*Department of Mechanical Engineering, Boston University, Boston, Massachusetts 02215, USA*
[2]*Photonics Center, Boston University, Boston, MA 02215, USA.*
[3]*Department of Biomedical Engineering, Boston University, Boston, Massachusetts 02215, USA*
[4]*Wyss Institute for Biologically Inspired Engineering, Harvard University, Boston, MA 02115, USA.*
[5]*Department of Biomedical Engineering, Boston University, Boston, MA 02215, USA.*
[6]*Division of Materials Science and Engineering, Boston University, Boston, Massachusetts 02215, USA*
[7]*Department of Electrical and Computer Engineering, Boston University, Boston, MA 02215, USA.*
[8]*Department of Physics, Boston University, Boston, MA 02215, USA.*

(Dated: March 7, 2021)

Contents

*Electronic mail:ekinci@bu.edu
†Electronic mail:aew1@bu.edu

I. FINITE ELEMENT SIMULATIONS

To estimate the relation between the applied pressure and the resulting displacements or the radial strains on the 20-μm-thick planar and 30-μm-thick curved PDMS cylindrical shells, finite element models of devices were developed using the Structural Mechanics module of the COMSOL Multiphysics Platform (version 5.5, COMSOL, Inc). The material properties used in the simulations for PDMS and PETA are listed in Table S1 [1, 2]. To model the adhesion between the PDMS and the glass surfaces, we applied a fixed boundary condition to the bottom surface of the structure. We kept the rest of the boundaries free to move, including the top PDMS anchor. The finite element model is meshed using free tetrahedral elements, with $\sim 2 \times 10^6$ elements generated. The smallest mesh elements are typically 0.3 μm in length.

A. Response to Applied Pressure

To estimate the effect of the external pressure differentials on the cylindrical shell, we applied Δp as a normal stress upon the outer wall of the PDMS shell. Fig S1A shows the deformation profiles of the 20-μm-thick planar and 30-μm-thick curved cylindrical shells under an applied vacuum of $\Delta p = -200$ mbar. This Δp induced a stretch in the radial direction with $\Delta r > 0$ as shown in Fig. S1A and C. In these color plots, only half of each structure with three attachment sites are shown for clarity. The thin solid lines indicate the initial positions of the walls and the attachment sites, which displace as a result of the deformation of the entire structure. We have observed that the deformation profile is more uniform across the 30-μm-thick curved cylindrical shells as compared to the 20-μm-thick planar ones. Another important point to emphasize is that there is negligible cage deformation compared to the shell deformations. To compare simulations with the calibration experiments, Δp is applied on the outer wall in the r direction, in 10 mbar increments ranging from -50 to 50 mbar . Subsequently, we extracted the resulting cage displacement Δr at the center of the cage ($z = h_m/2$) as a function of the applied Δp.

B. Response to Cardiac Twitches

Since the engineered cardiac microtissue is anchored by the attachment sites, we assume that the stubs of the cages experience the active contractile forces generated by the microtissue. Following this assumption, we modeled the contractile force by applying an outward normal stress on the stubs of the PETA cages (i.e., the surfaces of the small cylindrical structures in Fig. S1A-D) in $-r$ direction. Fig S1B and Fig S1D show the deformation profiles of the 20-μm-thick planar and 30-μm-thick curved cylindrical shells under applied tissue forces (σ = 40 kPa). We performed simulations for stress values between 0-10 kPa in 1 kPa increments, which is in the range of the experimentally observed values. Then, we extracted the resulting cage displacements at the center of the cage ($z = h_m/2$) as a function of the applied stress.

The results of all the simulations are shown in Fig. S1E. The absolute value of the cage displacements $|\Delta r|$ due to the externally applied pressure Δp are shown by open squares whereas those due to normal tissue stresses σ are shown by the filled circles. The reason that the slopes are different can be understood as follows. Δp acts upon the entire outer surface area of the PDMS shell, whereas σ acts only upon the surface of the cage stubs. Thus, the overall force is more for the case of Δp than σ. The slope difference between the 20-μm-thick planar and the 30-μm-thick curved shells is due to different thicknesses. In order to estimate the effective spring constant k_{eff} experienced by the tissue, we converted the simulated stress to force using $F = \sigma \pi {r_{cage}}^2$ (Fig. S2 and c.f. Fig 2C in main text).

TABLE S1: Properties of the materials used in the simulations.

Material	ρ (kg/m^3)	E (MPa)	ν
Polydimethylsiloxane (PDMS) [1]	970	2.2	0.48
Pentaerythritol triacrylate (PETA) [2]	1190	260	0.40

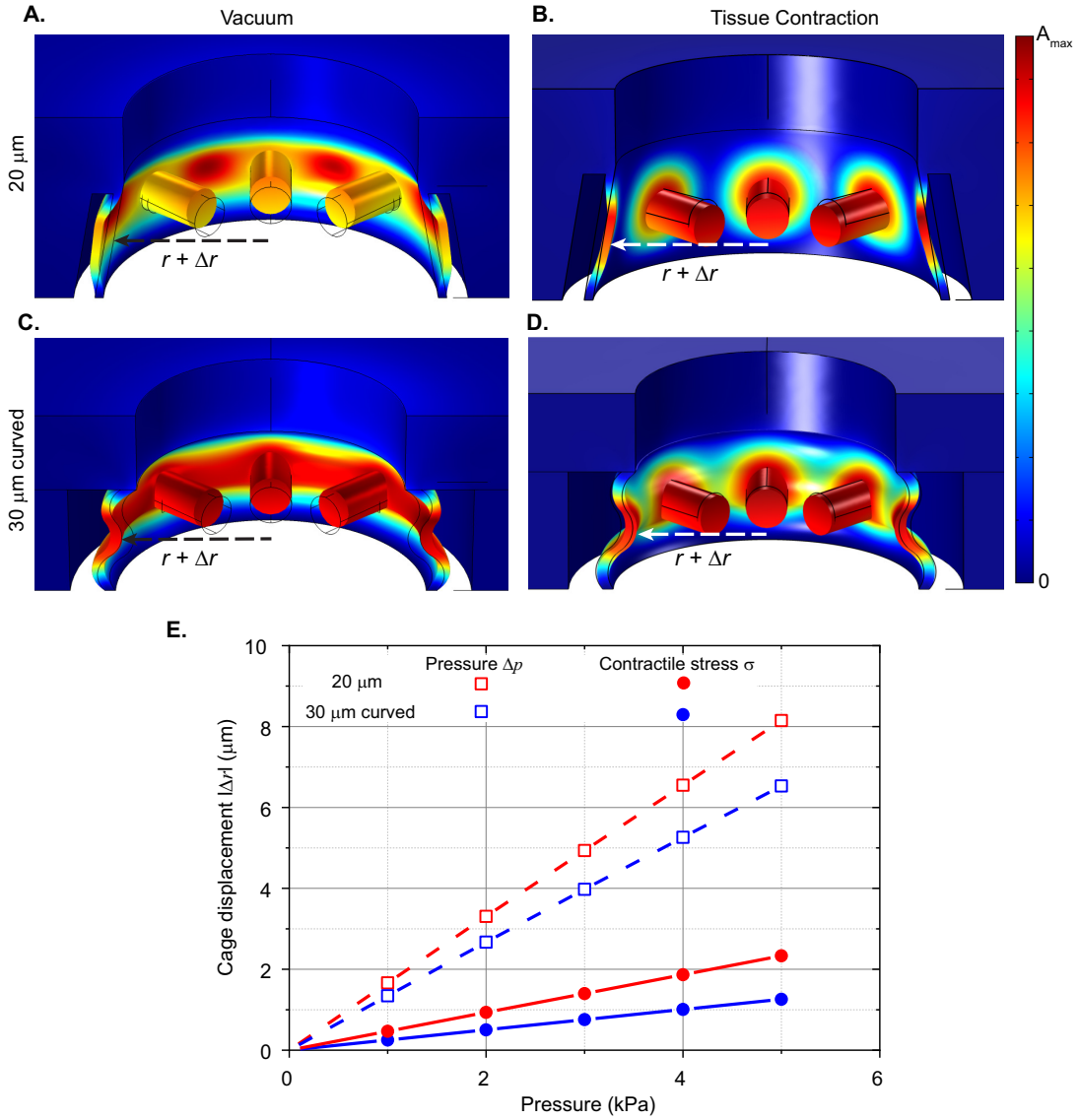

FIG. S1: Simulated deformation profile for the 20-μm-thick planar (A,B) and 30μm-thick-curved (C,D) PDMS shells under applied vacuum from annular chamber (A,C), and contractile stress σ applied from cage surfaces in normal direction (B,D). Cages on the sides are removed after the simulation for clarity (these are shown in Fig. 2B inset). Color represents the normalized displacement amplitude in the radial direction. E: Cage displacement as a function of applied external pressure Δp (dashed line) and contractile stress $\sigma = F/(\pi r^2)$.

II. ELECTRICAL MEASUREMENTS

A. Estimation of Electrical Resistance Change as a Function of Cage Displacement

Tissue generated contractile forces and the external pressure both act along the radial axis and induce bending of the cylindrical shell. Fig. S2 is an illustration of the bending of the shell. Here, width of the sensing microchannel changes by $\Delta r(\theta, z)$. Below, we derive an approximate relation between the average value of Δr and the electrical resistance change ΔR.

First, the deformation $\Delta r(\theta, z)$ will be assumed to be independent of θ as a simplification. Below, we discuss the validity of this assumption by exploring the deformation patterns in simulations. Since the top and the bottom of the microchannel are fixed, $\Delta r(z)$ should have an approximately parabolic deformation profile in the z direction due

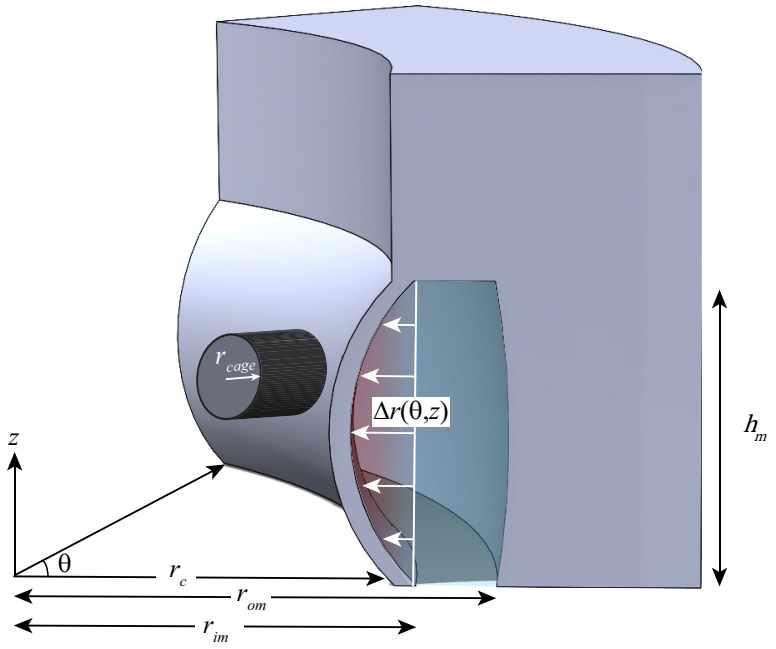

FIG. S2: An illustration of a sensing microchannel in cylindrical coordinates. $r_{om} - r_{im}$ and h_m are the width and height of the sensing microchannel respectively at $\Delta p = 0$ mbar, and $\theta \approx \pi/4$ rad . Pressure waves and forces exerted by the tissue similarly bends the PDMS shell, changing the microchannel width by $\Delta r(\theta, z)$.

to the applied pressure, resulting in an average wall deflection of [3]

$$\overline{\Delta r} \approx \frac{2}{3}\Delta r\,(z = h_m/2) \tag{S1}$$

Here, $\Delta r\,(z = h_m/2)$ is the maximum value of Δr. Note that the attachment sites are in the middle of the PDMS shell in the z direction (see Fig. 1C(iii-iv) and Fig. 2A in the main text), and $\Delta r\,(z = h_m/2)$ is the displacement that was measured optically in the experiments.

The angle subtended by the electrical sensing microchannel is approximately $\pi/4$ rad. The length of the microchannel can be approximated as $L \approx \frac{\pi(r_{om}+r_{im})}{8}$, where r_{im} and r_{om} are respectively the inner and outer radii of the microchannel as shown in Fig. S2.

Without any perturbation, the electrical resistance, $R_0 = \rho\frac{L}{A}$, of the microchannel of length L, cross-sectional area A and filled with a solution of resistivity ρ can be estimated as [4]

$$R_0 \approx \rho\frac{\pi\,(r_{om} + r_{im})}{8h(r_{om} - r_{im})} \tag{S2}$$

The forces on the walls perturb the channel inner radius to $r_{im} + \frac{2}{3}\Delta r$, which results in both a length change and a cross-sectional area change. This can be expressed as

$$R_0 + \Delta R \approx \rho\frac{\pi\left(r_{im} + r_{om} + \frac{2}{3}\Delta r\right)}{8h(r_{om} - r_{im} + \frac{2}{3}\Delta r)}. \tag{S3}$$

This expression can be approximated as

$$R_0 + \Delta R \approx \rho\frac{\pi\left(r_{om} + r_{im} + \frac{2}{3}\Delta r\right)}{8h(r_{om} - r_{im})}\left(1 - \frac{\frac{2}{3}\Delta r}{r_{om} - r_{im}}\right) \approx \rho\frac{\pi}{8h}\left[\frac{(r_{om} + r_{im})}{(r_{om} - r_{im})} + \frac{2\Delta r}{3(r_{om} - r_{im})}\right]\left[1 - \frac{2\Delta r}{3(r_{om} - r_{im})}\right] \tag{S4}$$

Keeping terms up to order two in Δr, we find the required expression for the resistance change ΔR as

$$\frac{\Delta R}{R_0} \approx -\frac{4}{3}\left[\frac{r_{im}\Delta r}{({r_{om}}^2 - {r_{im}}^2)} + \frac{(\Delta r)^2}{3({r_{om}}^2 - {r_{im}}^2)}\right] \tag{S5}$$

Eq. S5 captures the relationship between $\Delta R/R_0$ and Δr. Using the experimental linear calibration relationship between Δr and Δp in Eq. S5, we can estimate, as a check, the electrical responsivity $\mathcal{R}_e = \frac{\partial \Delta R}{R_0 \partial \Delta p}$ for the 20-µm-thick and 30-µm-thick devices. Using the linear dimensions of the devices, we found $\mathcal{R}_e \approx -1.65 \times 10^{-5}$ Pa^{-1} for the 20-µm-thick device and $\mathcal{R}_e \approx -8 \times 10^{-6}$ Pa^{-1} for the 30-µm-thick device. The theoretical $\mathcal{R}_e$ values found from Eq. S5 are roughly 2.5× larger than the experimental $\mathcal{R}_e$ values reported in Table 1 in main text. We suspect that this discrepancy is due to the parasitic contributions to the experimental value of R_0. The experimentally measured value of R_0 is also approximately a factor of 2.5 larger than the theoretically estimated resistance of the sensing region based on Eq. S2. Residual contact resistances increase the R_0, which lowers the relative resistance change $\Delta R/R_0$ and hence $\mathcal{R}_e$.

Lastly, we took a closer look at simulations to investigate the effect of different bending patterns resulting from (1) Δp applied on the outer wall of the shell and (2) stress σ exerted on the cage microstructures. Fig. S3 shows the simulated bending patterns of a 20-μm device from top at $z = h_m/2$, when the same force of magnitude $\approx$ 50 μN is applied as an external pressure (Fig. S3A) and as tissue contractions from each cage stub (Fig. S3B). These simulations show that the deformation profile is not uniform across the circumference of the shell at $z = h_m/2$. Since cage displacement Δr is the critical parameter for calibration, we focus on the sensing region and cage displacements. In Fig. S3C and D, we simulated two cases where cage displacements are approximately the same $\Delta r \approx 2.5-3$ μm with $\Delta p = 2$ kPa and $\sigma = 6$ kPa respectively. Even though the approximate cage displacements are the

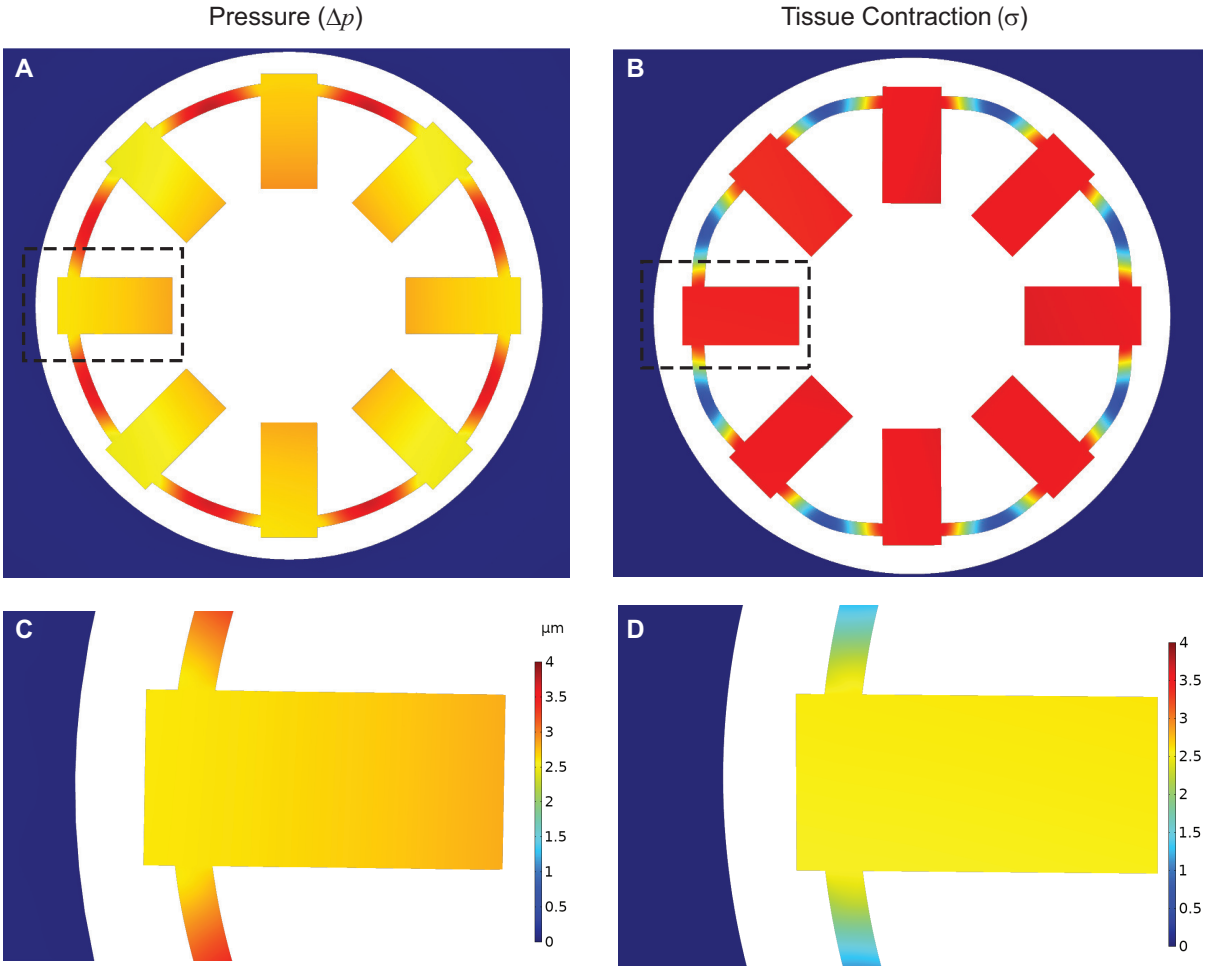

FIG. S3: Top view of simulated bending patterns of a 20 μm-thick cylindrical shell at $z = h/2$ upon applied external pressure (A,C) and tissue contractions (B,D). Top images show overall bending patterns that correspond to same applied force ($\approx$ 50 μN) from outer walls (A) and stubs of the cages (B), where colormap represents normalized amplitude of shell displacement. C and D display deformations experienced at the sensing site, as a response to pressure applied from outer walls ($\Delta p = 2$ kPa) and stubs of the cages ($\sigma = 6$ kPa) respectively. Even though cage displacement in both cases are approximately the same, $\Delta r(z = h/2) \approx 3$ μm, $\overline{\Delta r(\theta)_{\Delta p}} > \overline{\Delta r(\theta)_{\sigma}}$.

same for these two cases, the average displacements across the sensing region are different because of the complex θ dependence of $\Delta r(\theta)$. This clearly shows the limitation of the theoretical expressions derived above using the assumption of θ independence. We observed this difference experimentally when analyzing our electrical signals and when comparing forces exerted simultaneously both from the inside and outside of the seeding well (i.e., Fig. 5 in the main text). In these cases, we corrected the signals empirically, based on optical cage displacements.

B. Details of Electrical Resistance Measurement

Electrical resistance of the microchannel is monitored based on a four-wire measurement scheme using a lock-in amplifier (SR830, Stanford Research Systems). Circuit diagrams are shown in Figure S4.

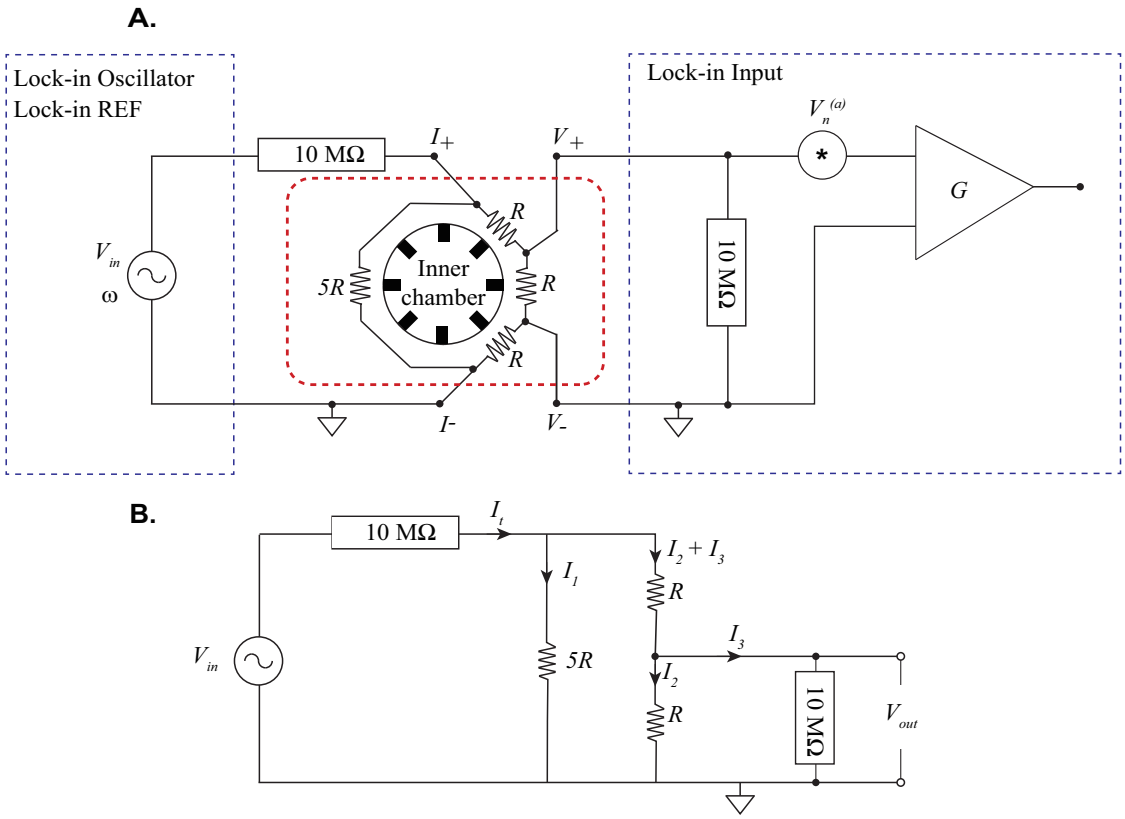

FIG. S4: Equivalent electrical circuit for the four wire resistive monitoring scheme. A: R is the electrical resistance of the outer microchannel that is being measured, it is $1/8^{th}$ of the annular microchannel. The blue dashed boxes represent the lock-in amplifier; V_{in} = 5 V, ω = 25 Hz, $V_n^{(a)}$ is the input noise voltage and G is the gain of the lock-in amplifier. Red dashed box represents the device. Approximately 500 nA AC current (I_{RMS}) goes through the device, and voltage drop on a microchannel that is adjacent to an attachment site is monitored locally for the displacement and force sensing. In measurement of a single device, approximately 40% of the injected current strays and loops around the annular microchannel. B: A simplified electrical circuit of a single device in order to estimate R from the measured voltage V_{out}.

Following Fig. S4B, we calculated the value of R from the measured voltage V_{out} by using basic circuit analysis:

$$R \approx \frac{V_{out}}{I_2} = \frac{V_{out}}{I_t - I_1 - I_3} \tag{S6}$$

Since $R \ll 10$ MΩ, the input current I_t can be approximated as $I_t \approx \frac{V_{in}-2V_{out}}{10\ \mathrm{M\Omega}}$. Likewise, $I_1 \approx \frac{2V_{out}}{5R}$ and $I_3 = \frac{V_{out}}{10\ \mathrm{M\Omega}}$. Combining all, R is approximately found as

$$R \approx \frac{7V_{out}}{5V_{in} - 15V_{out}} \times 10^7\ \Omega \tag{S7}$$

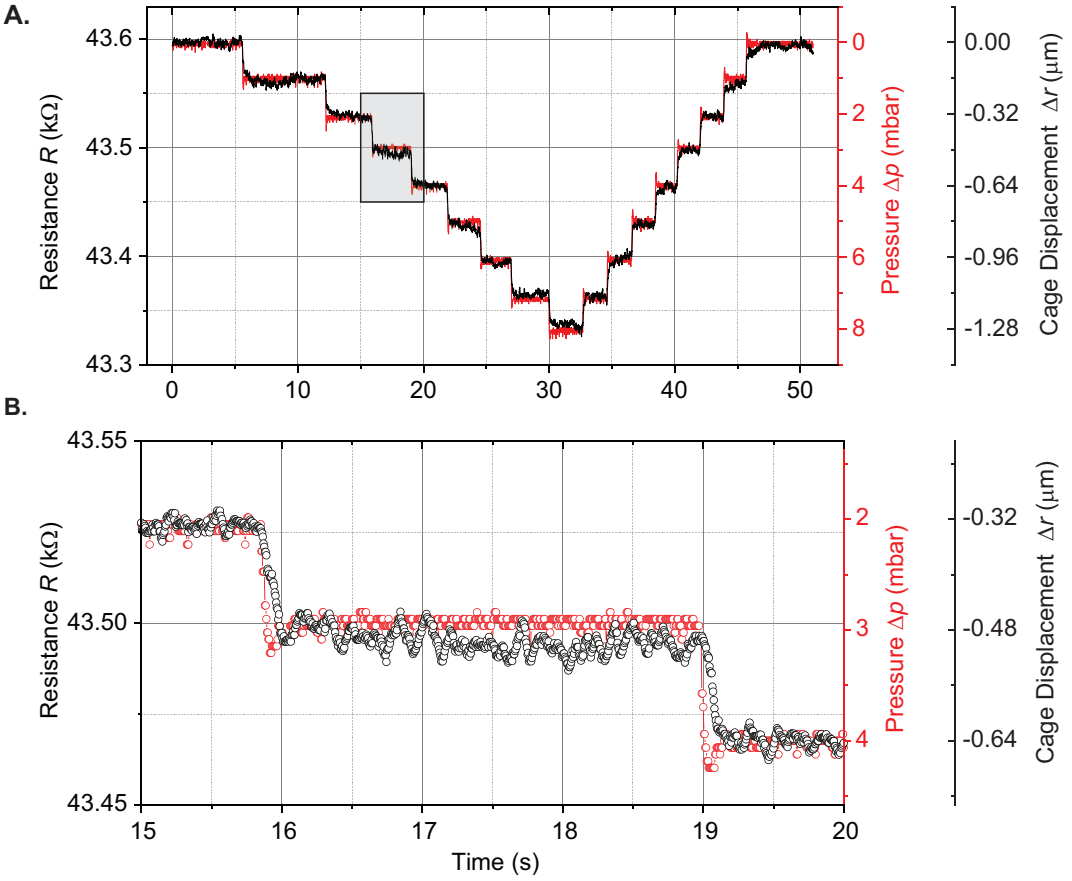

FIG. S5: Resolution of pressure regulation and resistance measurement from a device with 20 μm thick cylindrical shell. A: Resistance R (black) is tracked while pressure Δp (red) is varied between 0-8 mbar with 1 mbar increments. B: Close-up view to the highlighted area in A, where two 1 mbar steps are shown.

C. Estimation of Sensitivity Limits

Here, we briefly describe how we estimated the various sensitivity limits for the device. In order to to estimate the limits of resistance measurement, we determined the root-mean square (rms) resistance fluctuations normalized by the mean resistance R_0 value when the system was under equilibrium. In Fig. S5A, the equilibrium regions are on the plateaus. The rms value of normalized resistance fluctuations then gave us a minimum detectable resistance shift of $(\Delta R/R_0)_{min} \approx 6 \times 10^{-5}$ at a signal-to-noise ratio of 1. The equivalent bandwidth here was 15 Hz, which allows us to estimate a noise floor of 0.67 $\Omega/\mathrm{Hz}^{1/2}$. Note that by measuring longer, the sensitivity may be further improved but the value 0.67 $\Omega/\mathrm{Hz}^{1/2}$ establishes a helpful baseline. We estimate that our sensitivity is limited by the input noise of the lock-in, $V_n^{(a)}$, at 20× gain (≈ 100 nV/$\mathrm{Hz}^{1/2}$) and the Johnson noise of the resistor (≈ 30 nV/$\mathrm{Hz}^{1/2}$). Combining these two noise sources with V_{out} yield a theoretical noise floor of ≈ 0.3 $\Omega/\mathrm{Hz}^{1/2}$, which is not far from the experimentally measured noise floor.

By using the relation of $\mathcal{R}_e = \frac{\partial \Delta R}{R_0 \partial \Delta p}$, we converted the minimum detectable resistance to a minimum detectable pressure Δp_{min}. We estimated that $\Delta p_{min} \approx 8.8$ Pa/$\mathrm{Hz}^{1/2}$ for the 20-μm-thick planar device and $\Delta p_{min} \approx 12.8$ Pa/$\mathrm{Hz}^{1/2}$ for 30-μm-thick curved device. Next, we converted Δp_{min} to a minimum detectable cage displacement, Δr_{min}, by using the linear relation between Δr and Δp (see Fig. 2B in the main text). Lastly, Δr_{min} is converted to a minimum detectable force by $F = k_{eff} \Delta r$. The noise limits for 20 μm-thick planar and 30 μm-thick curved devices are summarized in Table 1 in the main text.

D. Available Bandwidth

The available bandwidth of the device can be inferred from the pulse excitation shown in Fig. 5A in the main text and Fig. S5B. The measured rise time (or the decay time) of $\tau \sim 0.1$ s can be converted to a bandwidth as $BW \approx \frac{0.35}{\tau}$. In Fig. S5B, the pressure readout from the sensor embedded in the piezoelectric micropump is tracked simultaneously with the electrical signal (red data trace). The pump outputs a step in a time scale of ~ 20 ms. Our analysis below suggests that the overall bandwidth of the system is probably limited by the intrinsic mechanical properties of the PDMS shells.

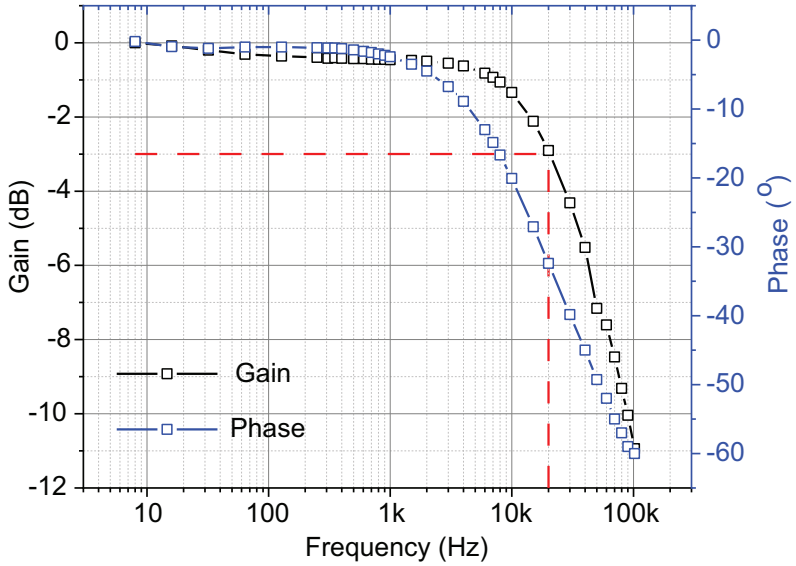

FIG. S6: Frequency response of a single device with 0.65 mm diameter Ag/AgCl wire electrodes. Output voltage corresponding to R is measured under same experimental conditions that is used in this study but different driving frequencies. Red dashed lines represent -3dB cutoff point, corresponding to a cutoff frequency of ~ 20 kHz.

1. *Electrical Bandwidth*

Fig. S6 shows the frequency response of a the electrical readout circuit. The electrical circuit in Fig. S4 is used for measurement, with the carrier frequency swept between 8 Hz - 100 kHz. Fig. S6 displays the magnitude (normalized to its low-frequency value in units of dB) and the phase shift of the output as a function of frequency. We observe that the cutoff frequency is $f_c \approx 20$ kHz, which corresponds to a time constant of $\tau \approx 8$ μs. This is the maximum available electrical bandwidth for the device and circuit in this study. Note that we took advantage of this electrical bandwidth when picking four different carrier frequencies $\gtrsim 200$ Hz during the parallel sensing endeavour. It is also worth emphasizing that we typically did not use the full bandwidth, instead we optimized the noise performance by using a lock-in time constant of $\sim 3-10$ ms. This bandwidth is still significantly larger than the observed bandwidth, indicating that the system is not limited by the response time of the electrical circuit.

2. *Mechanical Bandwidth*

Rise time of the pressure pulse applied by the pump appears to be $\sim$ 10-20 ms and is considerably faster than the observed mechanical response (Fig S5B, red curve vs. black curve). Assuming that there is negligible fluid flow in the system during the actuation and detection, pressure waves should propagate at the speed of sound. This should not cause a delay between the applied pressure and the observed mechanical response. Thus, it seems probable that the stress relaxation time of the PDMS limits the response time of the system [5]. Indeed, the observed mechanical bandwidth of the system in Fig S5 is on the same order with the reported relaxation times of other PDMS membrane based pneumatic actuators [6].

E. High-throughput Contractility Measurement and Electrical Cross-talk

Fig. S7 shows the electrical circuit diagram of the entire platform. Here, we estimate that ~ 40% of the injected current from each current source couples to other devices. Regardless, it is possible to avoid cross-talk and measure multiple devices in parallel if current is injected at different carrier frequencies and phase sensitive narrowband detection is employed. By using four custom-built portable lock-in amplifiers and taking advantage of the available electrical bandwidth (Fig. S6), we performed sensing at frequencies of 220 Hz, 260 Hz, 290 Hz and 320 Hz. We thus measured the active contractions from all four devices inside the platform. The equivalent bandwidth for these lock-in amplifiers were ≈ 10 Hz, thus the frequency band allocated to each sensor did not overlap with others.

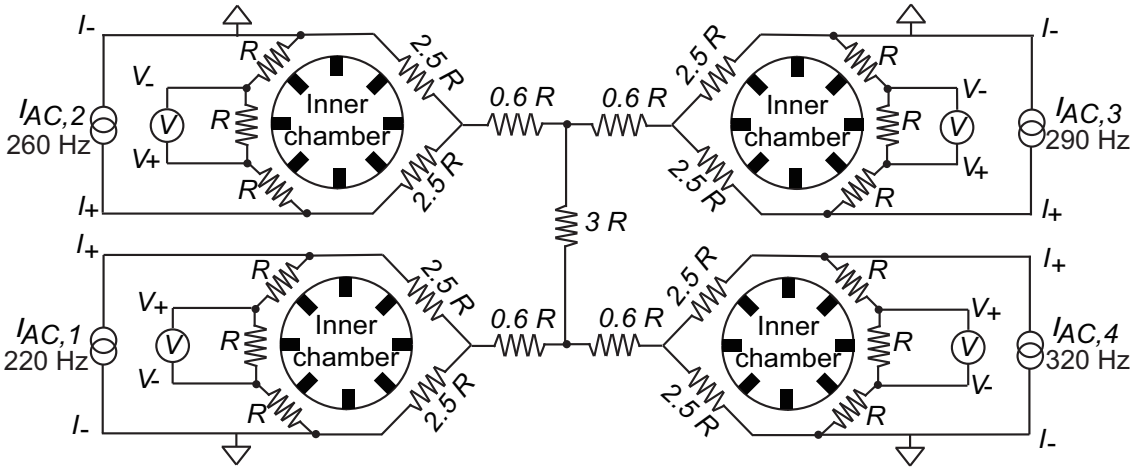

FIG. S7: Electrical circuit diagram of the overall platform and the experimental setup to measure contractile forces from all four devices simultaneously.

III. SOURCE OF NONLINEARITIES

A. Mechanical Nonlinearity

Based on the experimental results, we made a linear approximation between the applied pressure Δp and the displacement Δr (see Fig. 2B in main text) within the pressure range used in this study. Upon closer inspection, we observe that the 30-µm-curved shells are slightly more nonlinear and hysteretic compared to the 20-µm-planar shells. It appears that the curved geometry is slightly more responsive to the negative pressure than the positive pressure. The mechanical responsivity difference between $\Delta p < 0$ and $\Delta p > 0$ regimes is also observed in finite element simulations. It is possible to take into account this difference by using a linear fit for each regime at the expense of complexity. At extreme pressure differentials, however, it is clear from Movie S2 ($\Delta p \pm 400$ mbar) that stretching occurs as well as bending of the cylindrical shells. Hence, the combined effect of bending and stretching, as well as hyperelastic properties of PDMS, makes the relation between Δp and Δr nonlinear at the extreme limits.

B. Electrical Nonlinearity

After plugging in the dimensions for r_{om} and r_{im} and solving Eq. S5 with the nonlinear term $(\Delta R/R_0)_{NL}$, and without the nonlinear term, $(\Delta R/R_0)_L$, we observe that the relation between $\Delta R/R_0$ and Δr remains linear in the displacement range $-10\ \mu\text{m} < \Delta r < 10\ \mu\text{m}$: $\left|\frac{(\Delta R/R_0)_{NL}-(\Delta R/R_0)_L}{(\Delta R/R_0)_L} < 0.01\right|$. In our calibration and experiments, Δr remains in the range $-8\ \mu\text{m} < \Delta r < 8\ \mu\text{m}$. The tissue generated displacements were even smaller, $< 4\ \mu$m, making it acceptable to use a linear relation between $\Delta R/R_0$ and Δr. However, the resistance change also becomes nonlinear in extreme cases (such as that shown in Movie S2, where $\Delta r \approx \pm 60\ \mu$m).

IV. SUPPLEMENTARY MOVIES

A. Movie S1

Response of a cage to an externally applied triangular pressure waveform with a period of 5 s and approximate amplitude of ±50 mbar .

B. Movie S2

Maximum strains achievable with the platform. Actuation of the device with a 30-µm-curved shell with a triangular pressure waveform with a period of 10 s and amplitude of ±400 mbar. The shell is still durable and isolates the inner chamber from outer the chamber.

C. Movie S3

Attachment sites provide physical cues to define the geometry of the engineered cardiac microtissues. Spontaneous contractions from devices with attachment sites that are arranged in octagonal (left), pentagonal (middle) and rectangular (right) configurations.

D. Movie S4

Spontaneous contractions of cardiac microtissues in a 20-µm-thick planar (left) and a 30-µm-thick curved (right) devices, within the same platform.

E. Movie S5

Mechanical pacing of a microtissue in a device with a 20-µm-thick planar shell. Approximately 1.1% tensile strain is applied with the pump (−20 mbar, 250 ms long square pulses with 0.5 Hz frequency), while the engineered cardiac microtissue spontaneously beats at a frequency around 0.25 Hz, resulting in an approximately 0.75% compressive strain.

F. Movie S6

Spontaneous contractions of cardiac microtissues in all four devices on the same platform (left: 30-µm-thick curved devices, right: 20-µm-thick planar devices).

[1] I. D. Johnston, D. K. McCluskey, C. K. L. Tan, and M. C. Tracey, Journal of Micromechanics and Microengineering **24** (2014).
[2] R. Jayne, T. Stark, J. Reeves, D. Bishop, and A. White, Advanced Materials Technologies **3** (2018), ISSN 2365709X.
[3] O. Ozsun, V. Yakhot, and K. L. Ekinci, Journal of Fluid Mechanics **734** (2013).
[4] E. Weatherall and G. R. Willmott, Analyst **140**, 3318 (2015).
[5] S. Dogru, B. Aksoy, H. Bayraktar, and B. E. Alaca, Polymer Testing **69**, 375 (2018).
[6] Flexcell International Corporation, *Tension Cell Stretching Bioreactor System* (2020), URL `https://www.flexcellint.com/`.